nature physics

ARTICLES

PUBLISHED ONLINE: 12 SEPTEMBER 2016 | DOI: 10.1038/NPHYS3882

Nanotextured phase coexistence in the correlated insulator V_2O_3

A. S. McLeod[1]*, E. van Heumen[1,2], J. G. Ramirez[1†], S. Wang[1], T. Saerbeck[1†], S. Guenon[1], M. Goldflam[1], L. Anderegg[1], P. Kelly[1], A. Mueller[1], M. K. Liu[1†], Ivan K. Schuller[1] and D. N. Basov[1,3]

The insulator–metal transition remains among the most studied phenomena in correlated electron physics. However, the spontaneous formation of spatial patterns amidst insulator–metal phase coexistence remains poorly explored on the meso- and nanoscales. Here we present real-space evolution of the insulator–metal transition in a V_2O_3 thin film imaged at high spatial resolution by cryogenic near-field infrared microscopy. We resolve spontaneously nanotextured coexistence of metal and correlated Mott insulator phases near the insulator–metal transition (∼160–180 K) associated with percolation and an underlying structural phase transition. Augmented with macroscopic temperature-resolved X-ray diffraction measurements of the same film, a quantitative analysis of nano-infrared images acquired across the transition suggests decoupling of electronic and structural transformations. Persistent low-temperature metallicity is accompanied by unconventional critical behaviour, implicating the long-range Coulomb interaction as a driving force through the film's first-order insulator–metal transition.

The subtle interplay of charge, spin and orbital degrees of freedom in complex correlated oxides is known to result in strongly inhomogeneous phases, even in equilibrium[1]. In several families of correlated oxides including cuprates[2,3] and manganites[4–6], competing short- and long-range interactions give rise to emergent real-space patterns[7] that can provide fundamental clues to the principles underlying exotic behaviour of these systems. Spontaneous self-organization of coexistent phases remains largely unexplored in real space among many classes of materials exhibiting a first-order insulator–metal transition (IMT), attributable mostly to the absence of real-space probes capable of imaging the highly insulating side of the transition with nanoscale resolution. Enabled by nano-resolved infrared (nano-IR) imaging[8], we demonstrate how a self-organized real-space electronic nanotexture underlies a five-orders-of-magnitude change in resistivity through the IMT of V_2O_3. Furthermore, we resolve hitherto unreported characteristics of this correlated electron system, which challenge the conventional picture of an abrupt first-order insulator–metal transition.

The IMT in V_2O_3 from paramagnetic metal to low-temperature ($T \sim 160$ K) antiferromagnetic insulator (AFI)[9] arises from a thermally perturbed balance of entropy, kinetic energy and Coulomb repulsion among conduction electrons[10,11], leading to abrupt electron localization and a 0.7 eV energy gap[12]. These features appear intimately associated with a structural phase transition (SPT) from a corundum lattice to a lower symmetry monoclinic structure[10]. Increasingly refined studies have revealed unforeseen aspects of this transition[9,13,14], hypothesizing a more subtle phase diagram where real-space phase inhomogeneities play an essential role. The IMT and SPT have been found to decouple in the related compound VO_2, whereby a strongly correlated monoclinic metal emerges between low-temperature monoclinic insulating and high-temperature rutile metallic phases[15,16]. However, the exact role of Mott physics in VO_2 remains hotly debated, calling for a critical examination of real-space features entering the IMT of V_2O_3 at low T, where the role of electron localization by Coulomb repulsion is more conclusive[11,17–19].

We developed cryogenic infrared near-field (nano-IR) imaging (see Methods) to assess nanoscale phase inhomogeneity[20,21] emerging through the classic IMT in V_2O_3. Here, we imaged a 300-nm-thick highly oriented V_2O_3 thin film (Methods) at 25 nm resolution, revealing a spontaneous real-space nanotexture reflective of interactions governing the IMT. On first cooling into the transition, our local nano-optical probe resolves bi-directional stripes of the correlated insulator phase percolating through the parent paramagnetic metal, whereas macroscopic X-ray diffraction (XRD) of the same film reveals a concurrent corundum-to-monoclinic structural phase transition. Lower temperatures of the IMT render a complete structural transition, whereas metallic patches persist in an insulating background, implying that a novel monoclinic metal phase endures amidst the correlated insulator phase. Evolving real-space correlations and critical scaling among electronic domains suggest a crossover in the character of long-range interactions governing the electronic nanotexture: stripes stabilized by structural coexistence give way to a 'droplet' texture as predicted by frustrated mean-field theories that account for long-range Coulomb interactions[22–25].

Throughout this work we examine images of nano-IR signal S (Fig. 1a) normalized to an absolute reference through inclusion of a lithographically defined gold electrode within the imaging field of view (FOV) (not shown). We report details of nano-IR image processing in Supplementary Information II. Contrasts in the nano-IR signal form a reliable probe of local metallicity and therefore of the nanoscale IMT in correlated oxides (Methods)[15,20,21]. Here, we apply a colour scheme in which red represents high nano-IR signal, indicating metallic regions. In contrast, insulating domains where the dielectric function is positive present reduced nano-IR signal[20,21] and are represented in blue. Figure 1c displays a subset of images extracted from a fixed $20 \times 20\,\mu m^2$ FOV at select temperatures through a cooling and warming cycle measured with 920 cm^{-1}

[1]University of California San Diego, 9500 Gilman Drive, La Jolla, California 92093, USA. [2]University of Amsterdam, Sciencepark 904, 1098 XH Amsterdam, Netherlands. [3]Department of Physics, Columbia University, 538 West 120th Street New York, New York 10027, USA. †Present addresses: Universidad de los Andes, Bogotá 111711, Colombia (J.G.R.); Institut Laue-Langevin, 71 avenue des Martyrs, 38000 Grenoble, France (T.S.); Stony Brook University, Stony Brook, New York 11794, USA (M.K.L.). *e-mail: asmcleod@physics.ucsd.edu

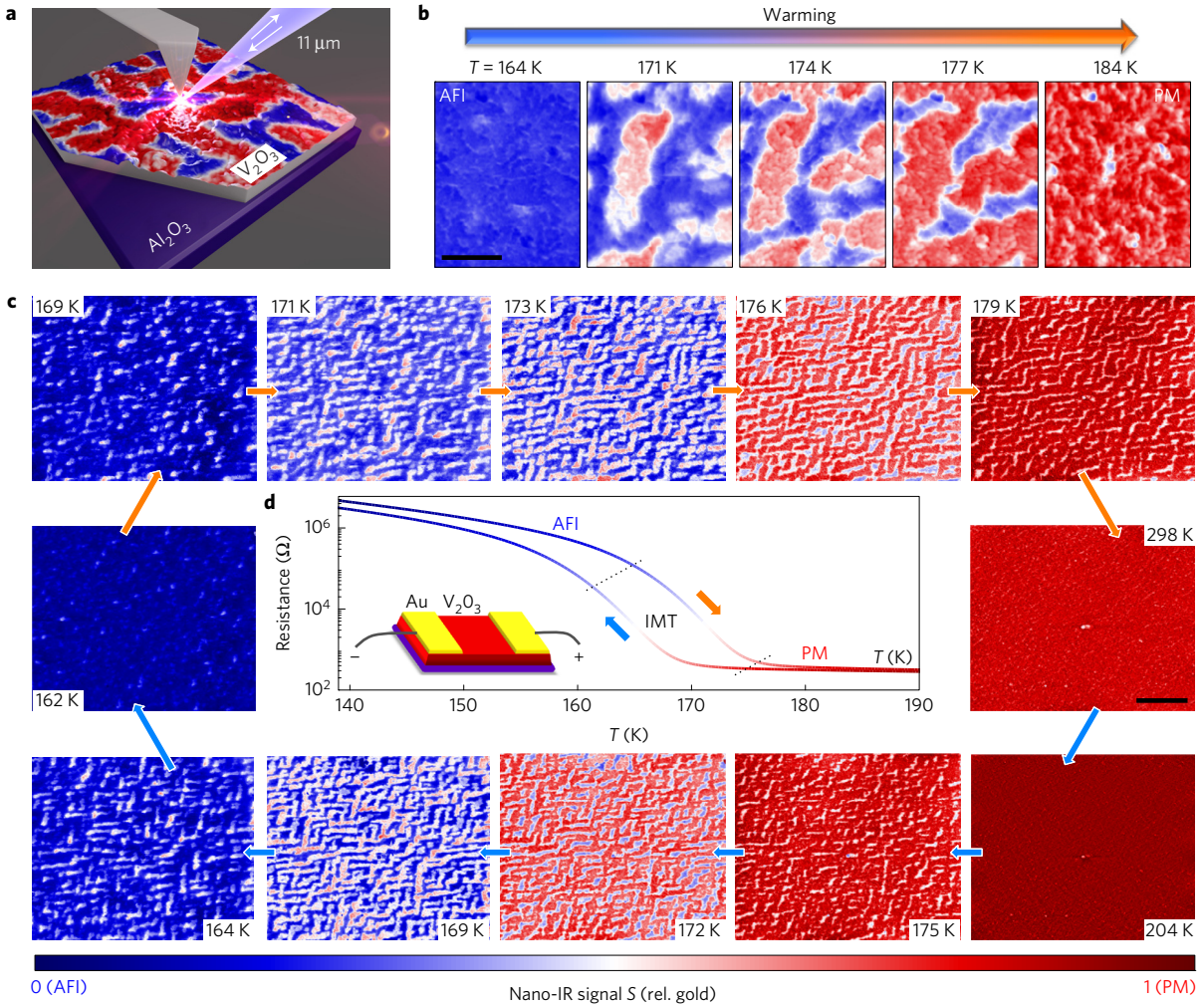

Figure 1 | Nano-IR imaging of the insulator–metal transition in V_2O_3. a, Schematic depiction of near-field microscopy of phase coexistence in a V_2O_3 thin film; nano-IR signal superimposed on film topography at 171 K (cooling). **b**, High-resolution co-localized near-field images of coexisting phases evolving on warming the film from the antiferromagnetic insulator (AFI) to paramagnetic metal (PM) phase; scale bar, 1 μm; colour scale as in **c**. **c**, Large-area co-localized nano-IR images of the electronic phase transition on cooling (blue arrows) and warming (orange arrows); scale bar, 5 μm. The colour scale (bottom) distinguishes metallic from insulating regions by their nano-IR signal *S*. **d**, Resistance of the film versus temperature on cooling (blue arrow) and warming (orange arrow); dotted lines demarcate the temperature range of phase coexistence in the insulator-to-metal transition (IMT). Inset: schematic arrangement of gold pads on the film surface used as *in situ* transport electrodes and for quantitative normalization of near-field images.

probe energy (~11 μm wavelength), probing predominantly the free-carrier optical (Drude) response of V_2O_3 according to far-field spectroscopy[11,12]. The most prominent features of these images are bi-directional stripes emerging spontaneously through the transition. On cooling from the metallic state (204 K), stripes of insulating material appear (175 K), grow (172 K) and fragment the metallic state (169 K), producing a striped pattern of metallicity. As the film resistance rapidly grows (160–170 K), metallic stripes disconnect (164 K), disorder into patches, and subsequently vanish into an insulating background (162 K). The transition follows a reverse trajectory on heating, albeit with a 6 K hysteresis. Images acquired at higher spatial resolution (25 nm pixels) are presented in Fig. 1b, clearly showing the growth of metallic domains in an insulating background on warming.

Images in Fig. 1 show that the IMT progresses on decreasing temperature through four successive stages: a homogeneous metallic state, a striped nanotexture of percolating electronic phase coexistence, an inhomogeneous insulating state populated with metallic patches, and a homogeneous correlated insulator state. The bipartite character of phase coexistence suggests a first-order phase transition with two characteristic values of the 'order parameter' (carrier density), in accord with conventional expectations for the Mott transition into an AFI state[10,11,26]. The majority of 'domain walls' between metallic and insulating regions are sharp within our spatial resolution (Fig. 1b). Most surprisingly, we note that nano-IR signal levels characteristic of the distinct phases themselves evolve gradually across the transition, uncovering bona fide thermal evolution of the electronic response, in contrast to a 'monolithic' phase transition between end-phases. Figure 2b quantifies the binary yet thermally evolving character of the transition via a histogram representation of nano-IR signals recorded at distinct temperatures on warming. Each bimodal nano-IR signal distribution consists of two distinct populations amidst the IMT. We identify these with 'insulating' (dashed blue curve) and 'metallic' (dashed red) sub-populations, each well fitted by an asymmetric (skew) normal distribution. Such binary behaviour has been previously observed in VO_2 (ref. 20).

Significant thermal evolution of the observed 'metallic phase' is attributable to continuous changes in optical conductivity of these domains. This evolution is consistent with a suppression of quasiparticle weight or pseudogap across the Mott IMT as predicted theoretically[27] and suggested by area-averaged spectroscopies of V_2O_3 (refs 12,13,26). Meanwhile, systematic temperature dependence of

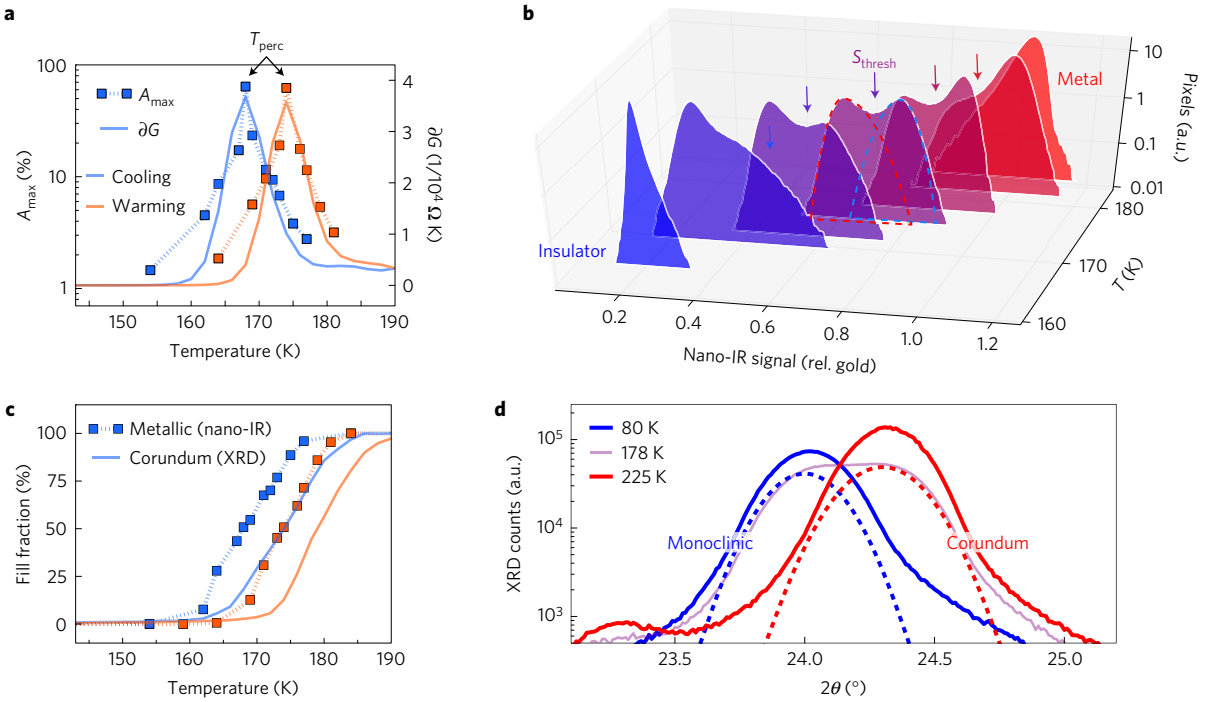

Figure 2 | Bimodal analysis of phase distributions in V_2O_3. a, Comparison of the size of the largest insulating or metallic cluster observed by near-field microscopy (A_{max}) against changes in film transport conductance per unit temperature ∂G for both cooling and warming; both metrics identify a coincident percolation threshold (T_{perc}). **b**, Histogram representation of near-field signal amplitudes (namely optical near-field reflectance) collected from the film at a subset of temperatures on warming from 164 K to 184 K, relative to an ideal metal (gold); an example fit to the distribution at 173 K by two asymmetric normal distributions reveals insulating (dashed blue) and metallic (dashed red) populations evolving with temperature, demarcated by a temperature-dependent threshold value of the near-field signal S_{thresh}, indicated from above by arrows; note vertical log scale. **c**, Thermometry-calibrated comparison of areal fill fractions for the metallic phase identified by nano-IR imaging against volumetric fractions for the high-temperature structural phase (corundum) identified by XRD; an anomalous thermal offset suggests persistent metallicity in the monoclinic structural phase. **d**, Bimodal decomposition of diffraction peaks measured by XRD admits measurement of structural fill fractions (Methods).

the nano-IR signal from 'insulating' regions is also noteworthy. An increase in their nano-optical signal while warming suggests a scenario whereby the insulating bandgap of the AFI state narrows through the IMT until becoming comparable to our probing energy (110 meV). Accordingly, calculations by cellular dynamical mean-field theory have proposed a narrow- to large-gap progression of the Mott insulating state in the phase-coexistent regime of the Hubbard model[28], and area-averaged optical probes also report an emergent pseudogap close to the IMT[12,26]. Moreover, mean-field treatments of photoexcitation in the related compound VO_2 find that changes in d-orbital occupancy can induce smooth collapse of the insulating gap preceding the abrupt IMT[29]. Our imaging results lend support to such scenarios among nanoscale regions in V_2O_3.

To bolster our attribution of insulating and metallic regions, we applied a binarization procedure (Methods) to analyse evolving cluster sizes and areal fractions of insulating and metallic phases. The dash-dotted curves of Fig. 2a obtained by this analysis display the area A_{max} (percentage of the FOV) of the largest cluster observed at each temperature. Figure 2a shows that A_{max} peaks at a temperature identifiable as the percolation threshold T_{perc}. At this temperature, the percolating phase switches in identity from 'metallic' to 'insulating' on cooling, or vice versa on warming. T_{perc} thus marks the percolation event, that is, the formation of an 'infinite' conducting pathway across the entire FOV and, by inference, the whole V_2O_3 film. Meanwhile, T_{perc} is also identifiable from the film's temperature-dependent electrical resistance R or conductance $G = R^{-1}$. Viewed as an effective circuit comprising parallel conductive pathways, the greatest change in film conductance is expected when the largest conductive pathway is formed or removed. Accordingly, the thermal derivative of the film conductance $\partial G \equiv (\mathrm{d}/\mathrm{d}T)R^{-1}$ (solid curves in Fig. 2a, obtained from *ex situ* resistance measurements) reaches a maximum value when the largest conducting pathway (spanning the film electrodes) is broken up. Our comparison between A_{max} and ∂G shows that percolation thresholds identified both *in* and *ex situ* agree to within 1 K and percolation occurs at 168 K (174 K) on cooling (warming).

Having established a nanoscale classification of metal and insulator, our binary images can reliably estimate the relative fill fractions of the two phases. Moreover, *ex situ* XRD measurements of the same V_2O_3 film reveal relative intensities of corundum and monoclinic diffraction peaks (Methods), allowing assessment of constituent structural phase fractions (Fig. 2d). Figure 2c compares the thermometry-calibrated (Supplementary Information III) metallic fraction (symbols) obtained by nano-IR to the corundum fraction (solid curves) obtained by XRD, revealing a 6 K thermal offset between electronic and structural transitions. Consistent with the percolation temperature identified *in* and *ex situ*, we find the metallic constituent is about 60% at 168 K while cooling, whereas the occupation of the corundum phase at this temperature remains ~25%, with an uncertainty of about 10%. This implies that some metallic regions must exhibit the monoclinic structure. Combined nano-IR and XRD measurements thus provide the first clear evidence that electronic and structural transitions can decouple in a V_2O_3 film.

Enabled by co-localized images at numerous temperatures, the binarizing threshold signal $S_{thresh}(T)$ pinpoints the temperature at which an individual image pixel switches from one electronic subpopulation to the other. This protocol defines a local insulator–metal transition temperature T_{IMT} resolved at each pixel with 25 nm precision (see also Supplementary Fig. 11). Figure 3a presents the thermal distribution of T_{IMT} from all image pixels, with consolidated

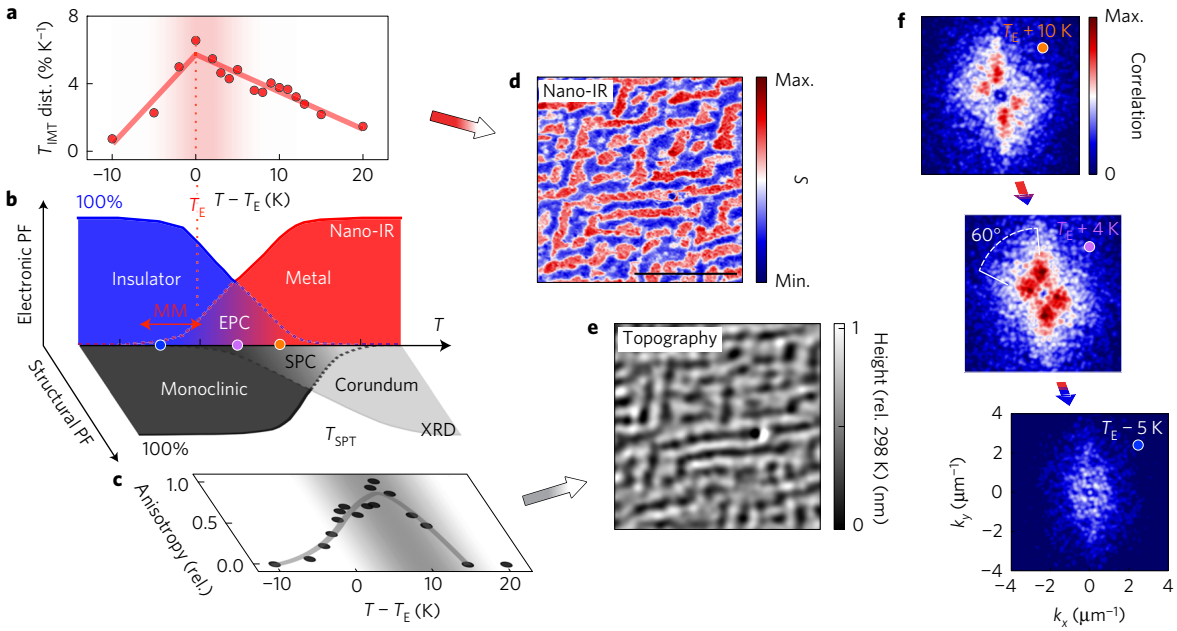

Figure 3 | Phase diagram for electronic and structural phases in thin-film V_2O_3. a, Distribution of insulator–metal transition temperatures T_{IMT} obtained as the fraction of observed pixels to transition per K; data from cooling and warming together. The peak in the transition indicates the characteristic transition temperature, T_E. **b**, Phase diagram presenting T-dependent fill phase fractions (PF) for electronic and structural phases (orthogonal axes) measured by nano-IR imaging and XRD. EPC, electronic phase coexistence; SPC, structural phase coexistence; MM, monoclinic metal. **c**, Directional anisotropy of electronic domain walls versus temperature as obtained from a binary insulator–metal classification of nano-IR image pixels; anisotropy maximizes abruptly at the structural phase transition temperature T_{SPT}, associating electronic anisotropy with 'guiding' by the SPT. **d**,**e**, Subset of nano-IR image at $T_E + 4$ K (warming) (**d**) compared with topographic corrugations (relative to 298 K) detected simultaneously by AFM (**e**); scale bar, 5 μm. **f**, Static structure factor (see text) of EPC measured near T_{SPT}, above T_E and below T_E, revealing preferred structural wavevectors emerging at 60° lateral separations; coloured dots indicate temperatures on the phase diagram panel (**b**).

data from cooling and warming (after removing the relative 6 K hysteresis). We identify the peak of the distribution with a characteristic temperature T_E for the electronic transition, equal to 164 K (169 K) for cooling (warming). The distribution shows that the IMT is most likely to occur at this temperature, a full 10 K below the structural phase transition temperature T_{SPT} where XRD indicates the SPT is most rapid (and where structural phases are detected at 50% fraction). Figure 3b presents a phase diagram comprised of phase fractions obtained from our data, with electronic and structural transitions shown on orthogonal axes. Moreover, the temperature range for the implied monoclinic metal is denoted in proximity to T_E.

The most striking feature in our images is the spontaneous formation of bi-directional stripes (Fig. 3d), suggesting an underlying organizational principle that could further elucidate the interplay between structural and electronic transitions. To characterize growth of these stripes, we quantify the extent of orientational anisotropy presented by domain walls as a function of temperature (Supplementary Information IV). Figure 3c reveals this anisotropy is maximized 10 K above T_E, matching well the structural phase transition temperature T_{SPT}. Likewise, we detect a pattern of <1 nm topographic corrugations (Fig. 3e) emerging at temperatures of the underlying SPT (Supplementary Fig. 9). Nanometre-scale surface buckling probably accompanies the differential unit cell volumes of coexisting structural domains[15,30]. These topographic features broadly coincide in real-space with the electronic nanotexture revealed by nano-IR (Fig. 3d,e), and their spatial cross-correlation is maximal at temperatures where the IMT and SPT overlap (Supplementary Fig. 9). Moreover, the striped electronic nanotexture exhibits periodicity that is best revealed through the temperature-dependent static structure factor, obtained as the spatial Fourier transform of the two-dimensional correlation function for phase coexistence (see Methods)[6,31]. Panels in Fig. 3f present the structure factor amplitude while cooling through three characteristic temperatures: close to T_{SPT} ($T_E + 10$ K), above T_E ($T_E + 4$ K), and below T_E ($T_E - 5$ K). Peaks in the structure factor that appear sharpest near T_{SPT} reflect preferential wavevectors for the spontaneous formation of anisotropic stripes. Spaced at 60° or 120° angular separations, these wavevectors explicitly reveal that three-fold rotational symmetry of the high-temperature corundum structure is broken bi-directionally by at least two monoclinic twin configurations[32]. A third crystallographic twin is expected but unobserved in our images, perhaps due to excess elastic mismatch of this domain orientation with the substrate. The mean length scale corresponding to wavevectors in Fig. 3f encodes the emergent periodicity resulting from phase coexistence in our film[33,34]. We associate this periodicity with a structural correlation length ξ_{struct}, as visualized in Fig. 4a, which shows a section of the correlation function perpendicular to stripes observed near T_{SPT} (see Methods and Supplementary Fig. 10). As shown in Fig. 4b, ξ_{struct} rises abruptly to a value of about 1.2 μm with a broad plateau centred also in the temperature range identified by XRD with the SPT.

The association of long-range spatial correlations and striped nanotexture with T_{SPT} is unmistakable. Indeed, a well-known real-space pattern of equilibrium structural phase coexistence can emerge spontaneously during a SPT, taking the form of a 'tweed' texture to minimize elastic strain energies among structural domains and the substrate[7,33,34]. Detailed studies of the sister compound VO_2 have revealed similar real-space patterns of structural phase coexistence tunable by temperature and by intrinsic or extrinsic stress[30,35]. Therefore, the observed temperature-dependent anisotropy and ξ_{struct} both suggest that the striped electronic nanotexture revealed by our images within this ∼20 K temperature window is largely a consequence of the IMT 'guided' by

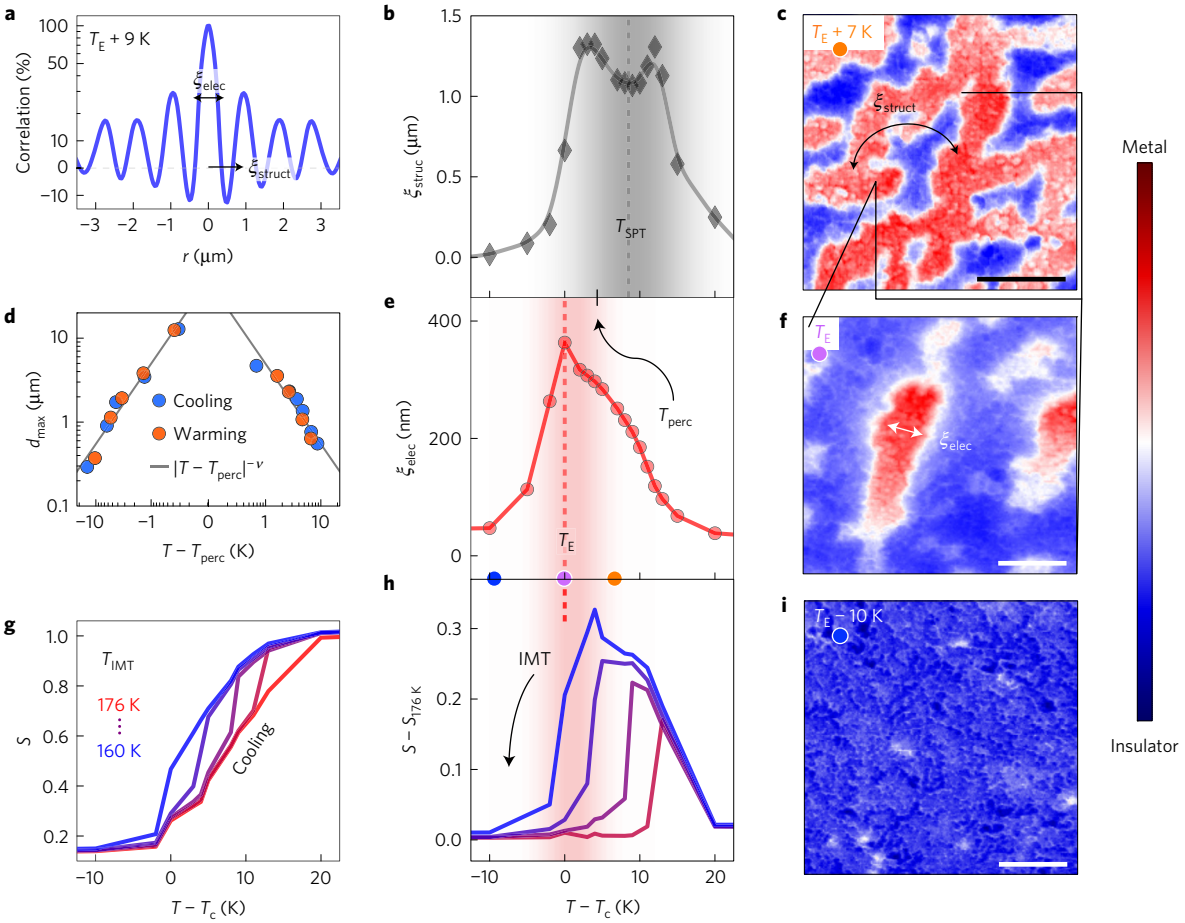

Figure 4 | Composite phenomena amidst the insulator–metal transition in V_2O_3. a, Trace from the image correlation function obtained 9 K above T_E, perpendicular to the direction of stripes; relevant correlation lengths are indicated. **b**, The structural correlation length associated with periodic correlations; ξ_{struct} plateaus at T_{SPT} and originates from structural phase coexistence. **c**,**f**,**i**, Acquisition temperatures for nano-IR images indicated by coloured dots in panel **e**. **c**, Indication of ξ_{struct} associated with real-space stripe periodicity; scale bar, 2 μm. **d**, Scale invariance of the largest electronic domain size d_{max}, fitting a power law with critical exponent $\nu \approx 1$ close to the percolation threshold temperature T_{perc}. **e**, The electronic correlation length associated with short-range correlations; ξ_{elec} peaks abruptly at T_E. **f**, Indication of ξ_{elec} associated with the characteristic size of metallic droplets; the FOV is a subset of panel **c**; scale bar, 1 μm. **g**, Average transition curves (nano-IR signal S versus T) acquired from pixels exhibiting insulator–metal transition temperatures $T_{IMT} = 176$ K (red) to 160 K (blue) on cooling. **h**, Curves from **g** after referencing to $T_{IMT} = 176$ K, revealing a first-order discontinuity in S down to $T_{IMT} = 160$ K. **i**, Monoclinic metallic matches are observed to persist even 10 K below T_E (~19 K below T_{SPT}); scale bar, 1 μm.

the underlying SPT. For temperatures near T_{SPT}, the lattice mismatch between monoclinic and corundum structural domains produces long-range elastic interactions (accommodation strain) governing the coexistence of electronic phases[33,34]. Additional nano-IR imaging of a thinner (100 nm) V_2O_3 film (Supplementary Information V and Supplementary Figs 12 and 13) reveals that ξ_{struct} is tunable with thickness in a fashion consistent with nanotexture mediated by accommodation strain.

As temperature decreases further towards T_E, we encounter clues concerning the character of monoclinic metallicity in this V_2O_3 film. First, we confirm that the low-temperature IMT proceeds by a clear first-order electronic phase transition even among persistent metallic domains. Figure 4g presents characteristic transition curves (S versus T) for loci of pixels that exhibit the same transition temperature T_{IMT} on cooling. Taking the transition curve corresponding to $T_{IMT} = 176$ K (red) for reference, Fig. 4h reveals a sharp first-order discontinuity in S for all T_{IMT}, and by implication, abrupt decrease in the Drude response. Sir Neville F. Mott's idealization of this IMT predicted such discontinuity on the basis of the long-range Coulomb interaction[10]. Dynamical mean-field theory studies of the Hubbard model have rigorously predicted a first-order Mott transition[11,24,36]. Such a first-order transition is now first evidenced among remnant metallic domains in the monoclinic phase. However, owing to further thermal evolution of the insulating phase observed throughout the IMT (Fig. 2b), we note that this first-order transition does not yet immediately yield the ultimate low-temperature AFI state appearing at $T < 160$ K.

The size and shape of persistent metallic domains is pertinent to the interactions governing their transition. The Landau theory for phase transitions holds that a thermally fluctuating balance between volumetric and surface free energies (associated in the Mott transition with electronic degrees of freedom[27]) among patches of the emerging phase will determine their spatial extent by way of short-range correlations[37]. We denote this spatial scale the electronic correlation length ξ_{elec}, and extract it at each temperature from the central full-width at half-maximum of the correlation function (Fig. 4a and see Methods). Figure 4e,f shows ξ_{elec}, which quantifies the characteristic isotropic length scale of electronic domains, reaching a maximum (~400 nm) at T_E. The growth and peak in ξ_{elec} near T_E reveals the tendency for metallic domains to form 'droplets' at these temperatures rather than stripes (Fig. 4f,i). This behaviour resembles the strong temperature dependence of spatial correlations that exhibit universal scaling near a critical point[17,37,38]. Similarly, we observe robust critical scaling through the

transition in the temperature dependence of the largest electronic domain size $d_{max} \equiv \sqrt{A_{max}}$ (A_{max} as presented in Fig. 2a) observed to scale as $|T - T_{perc}|^{-\nu}$ with $\nu = 0.96 \pm 0.07 \approx 1$ (Fig. 4d). Our directly resolved scaling shows quantitative agreement with the scale-invariant nucleation site density inferred from area-averaged optical studies of similar V_2O_3 films[39].

While considering the thermal evolution of these metallic domains, it is worth noting that our V_2O_3 film presents a metal–insulator transition among the cleanest (most abrupt) yet reported. Indeed, as evidenced by dissimilar maps of T_{IMT} for cooling and warming (Supplementary Fig. 11), positions of low-temperature metallic patches are largely spontaneous, implying a decoupling from pinning sites. Although critical scaling behaviours are unexpected amidst the first-order transition of a clean system, here they might be reconciled with predictions for frustrated phase separation in the Hubbard model. Below the Mott transition temperature, uniform band filling in the homogeneous state is proposed to become unstable at a fixed chemical potential, and the system phase-separates into regions with distinct charge density n associated with the insulating state at half band filling and a slightly doped metallic state[25]. This charge disproportionation Δn is theorized to reach a few per cent amidst the transition[24]. Consequently, long-ranged Coulomb interactions between domains are expected to penalize macroscopic charge separation, whereas interfacial domain wall energy σ favours few coexistent domains. This competition can produce a frustrated texture of droplet-shaped domains with characteristic size $d \sim (\sigma/\Delta n^2)^{1/3}$ whose correlation length $\xi_{elec} \propto \Delta n^{-1}$ is determined by screening[22,23,25,40]. The weak divergence of ξ_{elec} we observe in this temperature regime may arise from vanishing Δn as T approaches the probable IMT temperature T_E (ref. 24). Moreover, mean-field treatments of Coulomb-frustrated phase transitions have predicted power-law scaling of the characteristic droplet domain size with temperature, consistent with our observations for $d_{max}(T)$ (ref. 22). Most importantly, the intermediate appearance of a spontaneously nanotextured state across a first-order transition points to the relevance of long-range interactions that fundamentally prohibit a conventionally abrupt transition between end-phases[40].

Coulomb interactions can account for the crossover near T_E to a spontaneous droplet nanotexture that forms independently of the structural transition. Nevertheless, the origin for a novel monoclinic metal phase still invites explanation. Such a low-temperature metallic phase is reminiscent of reports for the related correlated oxide VO_2 (refs 15,16,20,31,41). Whereas a transient or pressure-induced monoclinic metal has been observed even in VO_2 single crystals[42,43], its more robust appearance in thinner extrinsically or epitaxially strained samples suggests a general mechanism decoupling the IMT from the SPT. For example, studies of the semi-infinite Hubbard model have predicted that interfacial metallicity stabilizes amidst a bulk Mott insulating state[44]. Meanwhile, X-ray absorption studies of V_2O_3 have identified inequivalent metallic states accessed through thermal and pressure-driven transitions[45] and have revealed a novel pressure-induced monoclinic metal phase[14], related perhaps to that detected here.

We propose that epitaxial strain and the consequent striped SPT nanotexture play a crucial role among films. Indeed, a stabilized intermediate electronic state with attributes of the high-temperature phase has previously been observed below the magnetoresistive transition temperature of manganite films[46]. This intermediate state was linked to accommodation strain from coexistent structural phases. Consequently, we speculate that an intermediate monoclinic metal phase in epitaxial V_2O_3 may be stabilized by epitaxial strain. Alternating regions of tensile and compressive accommodation strain in the striped nanotexture[15] may produce local deviations in the c/a lattice constant ratio. These deviations are expected to modulate orbital occupancy of both IMT end-phases[45,47], perhaps giving rise to their temperature-dependent optical response as observed here. Indeed, phase coexistence in a thinner V_2O_3 film, where effects of epitaxial strain are yet more prominent (see Supplementary Information) reveals even further 'coarsening' of the optical distinction between metal and insulator phases. Although tuning of orbital occupancy has been studied[29] and demonstrated in epitaxial VO_2 (ref. 48), such effects have not yet been investigated at the nanoscale. Moreover, the crossover observed here in V_2O_3 from striped (strain-mediated) to droplet nanotexture awaits observation in VO_2.

Associating the persistent low-temperature metallic phase of V_2O_3 with a strain-induced or Coulomb-frustrated phase implies novel real-space features of the insulator–metal transition, hitherto unexplored. Our study reveals that a rich interplay of short- and long-range interactions can lead to spontaneously nanotextured phase coexistence across the low-temperature insulator–metal transition in V_2O_3. Nano-optical imaging affirms that unexpectedly rich behaviours can underlie even this classic insulator–metal transition, while demanding modifications to the conventional phase diagram for strained epitaxial structures[10,17]. Low-temperature nano-spectroscopic probes and X-ray magnetic imaging will be essential to further elucidate the electronic character of intermediate phases emerging amidst the insulator–metal transition in V_2O_3 and other correlated oxides.

Methods

Methods, including statements of data availability and any associated accession codes and references, are available in the online version of this paper.

Received 14 April 2015; accepted 11 August 2016; published online 12 September 2016

References

1. Dagotto, E. Complexity in strongly correlated electronic systems. *Science* **309,** 257–262 (2005).
2. Tranquada, J. M., Sternlieb, B. J., Axe, J. D., Nakamura, Y. & Uchida, S. Evidence for stripe correlations of spins and holes in copper oxide superconductors. *Nature* **375,** 561–563 (1995).
3. Lawler, M. J. *et al*. Intra-unit-cell electronic nematicity of the high-T_c copper-oxide pseudogap states. *Nature* **466,** 347–351 (2010).
4. Uehara, M., Mori, S., Chen, C. H. & Cheong, S. W. Percolative phase separation underlies colossal magnetoresistance in mixed-valent manganites. *Nature* **399,** 560–563 (1999).
5. Ahn, K. H., Lookman, T. & Bishop, A. R. Strain-induced metal–insulator phase coexistence in perovskite manganites. *Nature* **428,** 401–404 (2004).
6. Lai, K. *et al*. Mesoscopic percolating resistance network in a strained manganite thin film. *Science* **329,** 190–193 (2010).
7. Seul, M. & Andelman, D. Domain shapes and patterns: the phenomenology of modulated phases. *Science* **267,** 476–483 (1995).
8. Knoll, B. & Keilmann, F. Near-field probing of vibrational absorption for chemical microscopy. *Nature* **399,** 134–137 (1999).
9. Frandsen, B. A. *et al*. Volume-wise destruction of the antiferromagnetic Mott insulating state through quantum tuning. *Nat. Commun.* **7,** 12519 (2016).
10. Imada, M., Fujimori, A. & Tokura, Y. Metal-insulator transitions. *Rev. Mod. Phys.* **70,** 1039 (1998).
11. Rozenberg, M. J. *et al*. Optical conductivity in Mott–Hubbard systems. *Phys. Rev. Lett.* **75,** 105 (1995).
12. Stewart, M. K. *et al*. Insulator-to-metal transition and correlated metallic state of V_2O_3 investigated by optical spectroscopy. *Phys. Rev. B* **85,** 205113 (2012).
13. Lupi, S. *et al*. A microscopic view on the Mott transition in chromium-doped V_2O_3. *Nat. Commun.* **1,** 105 (2010).
14. Ding, Y. *et al*. Novel high-pressure monoclinic metallic phase of V_2O_3. *Phys. Rev. Lett.* **112,** 056401 (2014).
15. Liu, M. K. *et al*. Anisotropic electronic state via spontaneous phase separation in strained vanadium dioxide films. *Phys. Rev. Lett.* **111,** 096602 (2013).
16. Kim, B.-J. *et al*. Micrometer X-ray diffraction study of VO_2 films: separation between metal–insulator transition and structural phase transition. *Phys. Rev. B* **77,** 235401 (2008).
17. Limelette, P. *et al*. Universality and critical behavior at the Mott transition. *Science* **302,** 89–92 (2003).

18. Guénon, S. *et al*. Electrical breakdown in a V_2O_3 device at the insulator-to-metal transition. *Europhys. Lett.* **101,** 57003 (2013).
19. Gebhard, F. *The Mott Metal–Insulator Transition: Models and Methods* (Springer Tracts in Modern Physics 137, Springer, 1997).
20. Qazilbash, M. M. *et al*. Mott transition in VO_2 revealed by infrared spectroscopy and nano-imaging. *Science* **318,** 1750–1753 (2007).
21. Atkin, J. M., Berweger, S., Jones, A. C. & Raschke, M. B. Nano-optical imaging and spectroscopy of order, phases, and domains in complex solids. *Adv. Phys.* **61,** 745–842 (2012).
22. Muratov, C. B. Theory of domain patterns in systems with long-range interactions of Coulomb type. *Phys. Rev. E* **66,** 066108 (2002).
23. Ortix, C., Lorenzana, J. & Di Castro, C. Universality classes for Coulomb frustrated phase separation. *Physica B* **404,** 499–502 (2009).
24. Macridin, A., Jarell, M. & Maier, T. Phase separation in the Hubbard model using the dynamical cluster approximation. *Phys. Rev. B* **74,** 085104 (2006).
25. Yee, C.-H. & Balents, L. Phase separation in doped Mott insulators. *Phys. Rev. X* **5,** 021007 (2015).
26. Baldassarre, L. *et al*. Quasiparticle evolution and pseudogap formation in V_2O_3: an infrared spectroscopy study. *Phys. Rev. B* **77,** 113107 (2008).
27. Georges, A., Krauth, W. & Rozenberg, M. J. Dynamical mean-field theory of strongly correlated fermion systems and the limit of infinite dimensions. *Rev. Mod. Phys.* **68,** 13 (1996).
28. Park, H., Haule, K. & Kotliar, G. Cluster dynamical mean field theory of the Mott transition. *Phys. Rev. Lett.* **101,** 186403 (2008).
29. He, Z. & Millis, A. J. Photoinduced phase transitions in narrow-gap Mott insulators: the case of VO_2. *Phys. Rev. B* **93,** 115126 (2016).
30. Tselev, A. *et al*. Interplay between ferroelastic and metal–insulator phase transitions in strained quasi-two-dimensional VO_2 nanoplatelets. *Nano Lett.* **10,** 2003–2011 (2010).
31. Laverock, J. *et al*. Direct observation of decoupled structural and electronic transitions and an ambient pressure monocliniclike metallic phase of VO_2. *Phys. Rev. Lett.* **113,** 216402 (2014).
32. Roytburd, A. L. Thermodynamics of polydomain heterostructures. I. Effect of macrostresses. *Appl. Phys. Lett.* **83,** 228–238 (1998).
33. Gao, Y. F., Lu, W. & Suo, Z. A mesophase transition in a binary monolayer on a solid surface. *Acta Mater.* **50,** 2297–2308 (2002).
34. Bratkovsky, A. M., Marais, S. C., Heine, V. & Salje, E. K. H. The theory of fluctuations and texture embryos in structural phase transitions mediated by strain. *J. Phys. Condens. Matter* **6,** 3679–3696 (1994).
35. Cao, J. *et al*. Strain engineering and one-dimensional organization of metal–insulator domains in single-crystal vanadium dioxide beams. *Nat. Nanotech.* **4,** 732–737 (2009).
36. Chitra, R. & Kotliar, G. Effect of long range Coulomb interactions on the Mott transition. *Phys. Rev. Lett.* **84,** 3678–3681 (2000).
37. Kadanoff, L. P. *et al*. Static phenomena near critical points: theory and experiment. *Rev. Mod. Phys.* **39,** 395–431 (1967).
38. Shuo, L. *et al*. Random field driven spatial complexity at the Mott transition in VO_2. *Phys. Rev. Lett.* **116,** 036401 (2016).
39. Abreu, E. *et al*. Dynamic conductivity scaling in photoexcited V_2O_3 thin films. *Phys. Rev. B* **92,** 085130 (2015).
40. Spivak, B. & Kivelson, S. A. Transport in two dimensional electronic micro-emulsions. *Ann. Phys.* **321,** 2071–2115 (2006).
41. Ramirez, J.-G., Sharoni, A., Dubi, Y., Gomez, M. E. & Schuller, I. K. First-order reversal curve measurements of the metal-insulator transition in VO_2: signatures of persistent metallic domains. *Phys. Rev. B* **79,** 235110 (2009).
42. Baum, P., Yang, D.-S. & Zewail, A. H. 4D visualization of transitional structures in phase transformations by electron diffraction. *Science* **318,** 788–792 (2007).
43. Arcangeletti, E. *et al*. Evidence of a pressure-induced metallization process in monoclinic VO_2. *Phys. Rev. Lett.* **98,** 196406 (2007).
44. Potthoff, M. & Nolting, W. Metallic surface of a Mott insulator–Mott insulating surface of a metal. *Phys. Rev. B* **60,** 7834 (1999).
45. Rodolakis, F. *et al*. Inequivalent routes across the Mott transition in V_2O_3 explored by X-ray absorption. *Phys. Rev. Lett.* **104,** 047401 (2010).
46. Podzorov, V., Kim, B. G., Kiryukhin, V., Gershenson, M. E. & Cheong, S.-W. Martensitic accommodation strain and the metal-insulator transition in manganites. *Phys. Rev. B* **64,** 140406 (2001).
47. Sakai, R., Limelette, P. & Funakubo, H. Transport properties and *c/a* ratio of V_2O_3 thin films grown on C- and R-plane sapphire substrates by pulsed laser deposition. *Appl. Phys. Lett.* **107,** 241901 (2015).
48. Aetukuri, N. B. *et al*. Control of the metal–insulator transition in vanadium dioxide by modifying orbital occupancy. *Nat. Phys.* **9,** 661–666 (2013).

Acknowledgements

A.S.M., E.v.H., M.G., L.A., P.K., A.M., M.K.L. and D.N.B. were supported by DOE-DE-SC0012375 and DOE-DE-SC0012592. J.G.R., S.W., T.S., S.G. and I.K.S. were supported by AFOSR Grant No. FA9550-12-1-0381. A.S.M. acknowledges support from a US Department of Energy Office of Science Graduate Fellowship (SCGF). Development of methods for cryogenic nano-infrared imaging is supported by ARO-w911NF-13-1-0210 and ONR-N00014-15-1-2671. D.N.B. is the Gordon and Betty Moore Foundation's Investigator in Quantum Materials award under the EPiQS Initiative through Grant GBMF4533. E.v.H. acknowledges the support of the US National Science Foundation I2CAM International Materials Institute Award, Grant DMR-0844115.

Author contributions

Experiments were conceived jointly by all authors. S.W. and J.G.R. grew the V_2O_3 film. A.S.M. and E.v.H. performed nano-IR measurements on the film, while J.G.R. and T.S. performed *ex situ* X-ray diffraction and resistance measurements. A.S.M., E.v.H., M.G., L.A. and P.K. developed the nano-IR instrumentation. All authors prepared the manuscript.

Additional information

Supplementary information is available in the online version of the paper. Reprints and permissions information is available online at www.nature.com/reprints. Correspondence and requests for materials should be addressed to A.S.M.

Competing financial interests

The authors declare no competing financial interests.

Methods

Cryogenic near-field optical nanoscopy. Scattering-type scanning near-field optical microscopy enables imaging of surface optical properties at variable temperatures[49] below the diffraction limit, with a resolution limited only by the geometric probe sharpness[21,50]. Here, we present images of the locally back-scattered near-field signal amplitude (abbreviated to nano-IR signal, or S) collected at low temperatures using a newly developed cryogenic near-field optical microscope based on low-temperature atomic force microscope from Attocube GmbH (Supplementary Information I and Supplementary Figs 1 and 2). Metallic regions where the d.c.-conductivity is high and the real part of the dielectric function is negative (at the probing IR frequency) yield high nano-IR signals comparable to that of good metals (namely gold). We recorded nano-IR images on cooling from room temperature across the IMT down to $T = 24$ K with a temperature interval of 2–4 K between 160 K and 180 K, followed by a similar number of measurements on warming to room temperature. Consistent results were also obtained on a 100 nm V_2O_3 film (Supplementary Information V and Supplementary Figs 12 and 13). All measurements were conducted in an ultrahigh-vacuum ($<10^{-8}$ mbar) environment to prevent surface contamination.

V_2O_3 films. This work focuses on a 300-nm-thick highly oriented V_2O_3 film (3 nm r.m.s. surface roughness, see Supplementary Information; surface topography presented in Supplementary Fig. 8) that displays a five-orders-of-magnitude increase in electrical resistance across the IMT from 180 K to 150 K (Fig. 1d) with a cooling/warming hysteresis of 6 K, characteristic of a first-order phase transition. Lithographically patterned gold pad electrodes on the film enabled *in situ* resistance measurements for accurate thermometry calibrations between nano-IR imaging and *ex situ* measurements of the same film (Supplementary Information). This film together with a similar 100 nm film were both epitaxially grown on (012)-plane sapphire substrate by radiofrequency magnetron sputtering from a V_2O_3 target (1.5′ diameter, >99.7%, ACI Alloys). The samples are prepared in a high-vacuum system with a base pressure of 1×10^{-7} torr. The substrate temperature was kept at 750 °C during the deposition. For the deposition of V_2O_3, 4 mtorr ultrahigh-purity (99.999%) Ar and 100 W radiofrequency power were used. These conditions yield a deposition rate of 0.67 Å s^{-1}. On the basis of X-ray diffraction characterization of the film, compressive strain from lattice mismatch between hexagonal lattice constants for room-temperature sapphire and V_2O_3, combined with stress relief by film buckling and granularity, induces lattice expansion along the film c axis and a concomitant increase in the c/a ratio relative to bulk crystals. Previous studies of sapphire-grown V_2O_3 films have equated this expansion with tensile hydrostatic chemical pressure attainable through chromium doping, affecting a putative decrease in bandwidth and increase in the Mott transition critical temperature[47]. Indeed, the transition temperature for our film is as much as 16 K higher than for bulk crystalline V_2O_3. Notably, previously grown films displayed characteristics similar to the best available single-crystal samples[12].

Determination of structural phase fractions by X-ray diffraction. We have determined the SPT temperature and the crystallographic phase fraction in our film by performing temperature-dependent X-ray diffraction (XRD) measurements. We measured the out-of-plane XRD of the rhombohedral (012) peak shifts from $2\theta = 24.30°$ above the SPT (300 K) to the monoclinic (011) $2\theta = 24.05°$ below it (100 K). The peaks were then fitted with two Gaussian curves; keeping fixed the 2θ values of the low- and high-temperature phases. The area under each Gaussian was normalized to the total area and the percentage volume fraction of each phase was thus obtained. The temperature T_{SPT} is identified as that where the structural transition is most likely, and incidentally where both phases are equally populated.

Binarization procedure. As presented in Fig. 2b, the histogram distributions of near-field signal values S measured at temperatures amidst the IMT are strongly bimodal. Each of these distributions is well fitted by a pair of skew normal (asymmetric Gaussian) distributions, which we associate with insulator and metal sub-populations. The point of intersection for these two normally distributed sub-populations (Fig. 2b) yields a threshold nano-IR signal that most probably distinguishes metal from insulator. We apply this temperature-dependent threshold $S_{thresh}(T)$ to assign individual pixels to the sub-populations of higher or lower conductivity (namely metal or insulator). Having thus binarized our images, we then rigorously identified both the individual electronic clusters (contiguous domains of the minority phase) and overall electronic phase fractions from our images, enabling the results of Figs 2a,c and 4d.

Correlation analysis. Informally, the correlation function $g(\delta \boldsymbol{r})$ of an image $I(\boldsymbol{r})$ (evaluated at lateral positions $\boldsymbol{r}$) expresses the level of statistical similarity between image features separated by a displacement $\delta \boldsymbol{r}$. Formally, the correlation function is given by[37]:

$$g(\delta \boldsymbol{r}) = \langle \delta I(\boldsymbol{r}), \delta I(\boldsymbol{r}+\delta \boldsymbol{r}) \rangle = \int d^2\boldsymbol{r} [I(\boldsymbol{r}) - \langle I(\boldsymbol{r}) \rangle] \left[I(\boldsymbol{r}+\delta \boldsymbol{r}) - \langle I(\boldsymbol{r}+\delta \boldsymbol{r}) \rangle \right] \quad (1)$$

Here $\langle \ldots \rangle$ indicates an areal average of the enclosed value. Appearance of the mean value $\langle I(\boldsymbol{r}) \rangle$ in equation (1) reflects that only image inhomogeneities ('features') are relevant for the characterization of spatial correlations. Equation (2) was used to compute the correlation function for each nano-IR image across the insulator–metal transition of our V_2O_3 film. Each correlation function was normalized to unity at $\delta \boldsymbol{r} = 0$, taken by construction to indicate 100% correlation.

The correlation function is known to reveal intrinsic periodicities more clearly within noisy data than would be possible to identify through direct inspection alone. We use this feature to identify periodicity in our nano-IR images, whose mean length scale we identify as ξ_{struct}. The characteristic wavevector for this periodicity $k = 2\pi/\xi_{struct}$ is most easily identified from the static structure factor $\tilde{g}(\boldsymbol{k})$, computed as the two-dimensional Fourier transform of the correlation function:

$$\tilde{g}(\boldsymbol{k}) = \frac{1}{L^2} \int_{-L/2}^{L/2} \mathrm{d}^2\boldsymbol{r} \mathrm{e}^{-i\boldsymbol{k}\cdot\boldsymbol{r}} g(\boldsymbol{r}) \quad (2)$$

Here, L denotes the size of the image over which the correlation function is computed. Meanwhile, the rotational average of the correlation function (yielding $g(r)$, evaluated at displacement magnitude r alone) was used to identify ξ_{elec} according to its central full-width at half-maximum. This correlation length reflects the typical scale for statistical correlations to locally decay by e^{-1} and corresponds intuitively with the average characteristic dimension of image inhomogeneities. In our case, these comprise puddles of the minority electronic phase—whether insulating in character above the percolation temperature, or metallic below. The weakly 'divergent' character of ξ_{elec} revealed by our correlation analysis and the thermal scaling of metallic 'droplet' sizes both resemble the phenomenology of Landau theory for scale-invariant spatial fluctuations proximate to the critical point of a continuous phase transition[37]. In the case of a first-order phase transition, long-range interactions can provide an alternative route to critical behaviour[22].

Data availability. The data that support the findings of this study are available from the corresponding author on request.

References

49. Yang, H. U., Hevestreit, E., Josberger, E. E. & Raschke, M. B. A cryogenic scattering-type scanning near-field optical microscope. *Rev. Sci. Instrum.* **84,** 023701 (2013).
50. Hillenbrand, R. & Keilmann, F. Complex optical constants on a subwavelength scale. *Phys. Rev. Lett.* **85,** 3029–3032 (2000).